Eur. Phys. J. B (2019) 92: 163
https://doi.org/10.1140/epjb/e2019-100149-9

THE EUROPEAN PHYSICAL JOURNAL B

Regular Article

Cation ordering, ferrimagnetism and ferroelectric relaxor behavior in $Pb(Fe_{1-x}Sc_x)_{2/3}W_{1/3}O_3$ solid solutions*

Sergey A. Ivanov[1,2], Premysl Beran[3], Alexandr A. Bush[4], Tapati Sarkar[2], Samrand Shafeie[5], Duo Wang[6], Biplab Sanyal[6], Olle Eriksson[6], Martin Sahlberg[5], Yaroslav Kvashnin[6], Roland Tellgren[5], Per Nordblad[2], and Roland Mathieu[2,a]

[1] Center of Materials Science, Karpov Institute of Physical Chemistry, Vorontsovo Pole, 10, Moscow 105064, Russia
[2] Department of Engineering Sciences, Uppsala University, Box 534, 751 21 Uppsala, Sweden
[3] Nuclear Physics Institute, CAS, Rez, Czech Republic
[4] Moscow Technological University, Moscow 119454, Russia
[5] Department of Chemistry, Ångstrom Laboratory, Uppsala University, Box 538, 751 21 Uppsala, Sweden
[6] Department of Physics and Astronomy, Uppsala University, Box 516, 751 20 Uppsala, Sweden

Received 14 March 2019 / Received in final form 25 May 2019
Published online 1 August 2019

Abstract. Ceramic samples of the multiferroic perovskite $Pb(Fe_{1-x}Sc_x)_{2/3}W_{1/3}O_3$ with $0 \leq x \leq 0.4$ have been synthesized using a conventional solid-state reaction method, and investigated experimentally and theoretically using first-principle calculations. Rietveld analyses of joint synchrotron X-ray and neutron diffraction patterns show the formation of a pure crystalline phase with cubic ($Fm\bar{3}m$) structure with partial ordering in the *B*-sites. The replacement of Fe by Sc leads to the increase of the cation order between the B' and B'' sites. As the non-magnetic Sc^{3+} ions replace the magnetic Fe^{3+} cations, the antiferromagnetic state of $PbFe_{2/3}W_{1/3}O_3$ is turned into a ferrimagnetic state reflecting the different magnitude of the magnetic moments on the B' and B'' sites. The materials remain ferroelectric relaxors with increasing Sc content. Results from experiments on annealed and quenched samples show that the cooling rate after high temperature annealing controls the degree of cationic order in $Pb(Fe_{1-x}Sc_x)_{2/3}W_{1/3}O_3$ and possibly also in the undoped $PbFe_{2/3}W_{1/3}O_3$.

1 Introduction

The search for new multiferroic (MF) materials is driven by the hope to find materials that can be used for the transformation of a magnetic signal to an electric response, and vice versa [1–3]. The most promising candidate materials for such applications are double perovskites [4–6]. $PbFe_{2/3}W_{1/3}O_3$ (PFWO) belongs to the family of Pb-based 2:1 perovskites combining magnetically active Fe^{3+} cations with ferroelectrically active W^{6+} cations [7,8]. PFWO exhibits relaxor ferroelectric [9–12] behaviour between 150 K and 200 K and antiferromagnetic (AFM) order with a Néel temperature TN of approximately 350 K. An interesting peculiarity of the PFWO system in comparison with other MF perovskites is that the presence of Fe^{3+} with an occupancy of 2/3 on the B-octahedral sites of the perovskite cells leads to one of the highest magnetic ordering temperature in double perovskites [5]. It is generally accepted that the Fe^{3+} and the W^{6+} cations are nearly randomly distributed at the *B*-site so that there is no long-range structural ordering [9–11]. Although PFWO remains in focus of the attention of the scientific MF community [13–16], it has still limited use in applications due to several reasons such as the formation of secondary phases during synthesis, weak magnetic characteristics, and a wide difference in ferroic transition temperatures [14,16]. In the last few decades, several attempts have been made to modify the properties of PFWO by substitutions at the *A* or (and) *B* crystallographic sites. A long-range ferroelectric order may be introduced by alloying PFWO with rare earth elements and transition metals. Results from studies using various solid solutions have been reported, for instance, by A-site substitution with Ba^{2+}, Sr^{2+}, Ca^{2+} and La^{3+} [17–21] and B-site substitution with Ni^{2+}, Mg^{2+}, Co^{2+}, Cr^{3+}, Mn^{3+}, Ti^{4+}, Zr^{4+} [21–37], or addition of $PbTiO_3$ [38–40]. These studies show that cation doping is an effective method to tune the magnetic and dielectric properties of PFWO.

One way to tune the magnetic properties of PFWO is to control the degree of ordering of Fe^{3+} and W^{6+} cations as this leads to a change of the number of magnetic ions in neighbouring cells. Promising results were reported in the case of Sc doping [41,42]. Furthermore, although major advances have been made in optimizing PFWO for a variety of applications, several fundamental aspects of

* Supplementary material in the form of one pdf file available from the Journal web page at
https://doi.org/10.1140/epjb/e2019-100149-9

[a] e-mail: roland.mathieu@angstrom.uu.se

their behaviour, in particular, the nature of the compositional ordering and its relation to the relaxor properties, have remained poorly defined and somewhat controversial [43–46]. The aim of the present work is to clarify the effect of substitution of Sc^{3+} for Fe^{3+} on the structural, magnetic, and dielectric properties of PFWO. Phase-pure, stoichiometric $Pb(Fe_{1-x}Sc_x)_{2/3}W_{1/3}O_3$ (PFSWO) samples were prepared. The structural, dielectric and magnetic properties of quenched PFSWO samples have been investigated using a combination of X-ray synchrotron and neutron powder diffraction, magnetometry, dielectric spectroscopy and electron microscopy, with focus on compositions $x = 0.1$, 0.2, 0.3 and 0.4. Doping with Sc for Fe in PFWO is found to promote the ordering of the Fe(Sc) and W cations on the B site and large excess moments accompanied by narrowing of the ferroelectric relaxation. Cation ordering in the undoped PFWO system is also discussed.

2 Experimental

2.1 Sample preparation

Ceramic samples of $Pb(Fe_{1-x}Sc_x)_{2/3}W_{1/3}O_3$ ($0 \leq x \leq 1$) (PFSWO) were prepared by a traditional multiple-step solid state reaction method in air and vacuum (10^{-2} atm) [47,48]. Stoichiometric amounts of reagent grade PbO, Fe_2O_3, Sc_2O_3 and WO_3 of purity 99.9% or higher, were used as precursors. The mixtures were ground by hand in an agate mortar and pressed into pellets, which were placed in a platinum crucible covered with a lid and then preheated for 4 h at 800 °C. A PbO-rich atmosphere was maintained to prevent Pb volatilization during sintering. This was achieved by performing the synthesis in closed crucibles, placing inside an additional amount of PbO (up to 10 wt.%). The samples were weighed before and after heat treatment to determine possible Pb loss due to evaporation. In all cases, the weight difference was negligible (<0.01%). With increasing Sc content, the firing temperature was increased from 850 to 970 °C. The samples were fired for a total of 10 h and then furnace-cooled. The firing products were ground into powders, which were pressed at 15 MPa into cylindrical disk shapes, 10 mm in diameter and 1–3 mm in thickness. These disks were then sintered between 850 and 970 °C for 4 h. The reaction mixtures were examined using XRPD patterns and the reaction was judged to be complete when the pattern could be indexed as a single phase or when further heating caused no discernible change in the diffraction profile. Before any measurements, a surface layer was removed from the samples by sandpaper and possible secondary phases were leached away in warm 10% diluted HNO_3.

A series of PFWSO pellets of composition $x = 0.1$, 0.2, 0.3, and 0.4 were subjected to special heat treatment. In the final stage of the preparation, they were kept at between 850 and 970 °C for 76 h and then cooled by different protocols. One set of pellets was removed from the furnace at the above mentioned temperatures and rapidly cooled to 295 K by placing them on a massive steel plate (quenched samples) and another set was slowly cooled (1 °C/min) down to 295 K (annealed samples). The present study focuses on the properties of the quenched samples of PFSWO. Results on the annealed systems were recently published in [47,48].

The chemical composition of the samples was checked by scanning electron microscopy (SEM), and X-ray energy dispersive spectroscopy (EDS) analyses. Mössbauer spectroscopy, and dielectric and magnetic measurements were performed on selected samples (see Supplemental Materials for experimental details).

2.2 X-ray powder diffraction

The phase formation and impurity levels of the synthesized ceramics were examined by using X-ray powder diffraction (XRPD). The patterns were obtained with a D-5000 diffractometer using Cu K_α radiation. The ceramic samples of PFSWO were crushed into powder in an agate mortar and suspended in ethanol. A Si substrate was covered with several drops of the resulting suspension, leaving randomly oriented crystallites after drying. The XRPD data for Rietveld analysis were collected at room temperature on a Bruker D8 Advance diffractometer (Vantec position-sensitive detector, Ge-monochromatized Cu $K_{\alpha 1}$ radiation, Bragg-Brentano geometry, DIFFRACT plus software) in the 2θ range 10–152° with a step size of 0.02° (counting time was 15 s per step). The slit system was selected to ensure that the X-ray beam was completely within the sample for all 2θ angles. The XRPD patterns were analysed with the Rietveld profile method using the FULLPROF program [49]. The diffraction peaks were described by a pseudo-Voigt profile function, with a Lorentzian contribution to the Gaussian peak shape. A peak asymmetry correction was made for angles below 35° (2θ). Background intensities were estimated by interpolating between up to 40 and 50 selected points.

2.3 Synchrotron X-ray powder diffraction

Synchrotron X-ray powder diffraction (SXRPD) was carried out at the P02.1 beamline at DESY in Hamburg, Germany [50]. The wavelength was determined as 0.207109 Å by using a Si standard. A PerkinElmer XRD1621 detector and an exposure time of 1 s per diffraction pattern, and summing 10 patterns, was used for data collection during the experiments. The samples were measured in 0.5 mm quartz capillaries, using a sample spinner. The Fit2d program was used for data reduction from 2D images to 1D diffraction patterns [51].

2.4 Neutron powder diffraction (NPD)

Due to significantly different neutron scattering length of Fe, Sc and W (b_{Fe} = 9.45 fm, b_{Sc} = 12.29 fm, b_W = 4.86 fm) [52], NPD technique is an appropriate tool to analyse the occupation order on the B-site of the studied perovskites. The neutron scattering length of oxygen (b_O = 5.805 fm) is comparable to those of the heavy atoms and NPD provides accurate information on its position and stoichiometry. NPD patterns at selected temperatures within the 4–900 K interval were collected on the NPD instrument MEREDIT@NPI (Nuclear Physics Institute

CAS, Czech Republic) using a neutron wavelength of 1.46 Å. Powder samples in vanadium containers were placed inside a close-cycle cryostat or a vacuum furnace for measurements from 4 K to room temperature and from room temperature to 900 K, respectively. In all cases data were collected in an angular 2θ range from 4 to 144° with a step of 0.08°. An instrument resolution function (IRF) describing the instrument profile function obtained from pattern fitting of a SiO_2 standard using the same monochromator setting was used during the Rietveld refinement. The NPD experimental diffraction patterns were analysed with the Rietveld profile method using the FULLPROF program [49]. A peak asymmetry correction was made for angles below 65° (2θ). Background intensities were estimated by interpolating between up to 50 selected points. Symmetry analysis to determine possible spin arrangements was done using the Bilbao Crystalographic Server [53] and BASIREPS software [49]. All available magnetic symmetries were checked by fitting of low temperature NPD data. Additional NPD data for quenched PFWO sample were collected at the Swedish Research reactor R2 at Studsvik at 325, 350, and 450 K (a wavelength 1.470 Å). Corrections for absorption effects were subsequently carried out in the Rietveld refinements, utilizing the empirical value $m_R = 0.083\,\mathrm{cm}^{-1}$. The step-scan covered a 2θ-range 4–139.928 with a step-length of 0.088. Each experiment lasted for 15 h.

Since Mössbauer spectroscopy has provided strong support for the existence of Fe in the trivalent state in PFSWO samples [47,54], the magnetic structure was refined using a calculation of magnetic moments for selected Fe^{3+} cations within the nuclear model. Several magnetic models were tried in the refinement, each employing one additional refinement parameter, corresponding to the magnitude of the magnetic moment.

2.5 Joint refinement of SXRPD and NPD patterns

To resolve the complexity of calculation of atomic ratio on two independent crystallographic sites occupied by three atoms, a joint Rietveld refinement of SXRPD and NPD data at room temperature was employed. X-ray diffraction signal from *B*-sites is dominated by W atoms whereas the neutron signal is dominated by Sc and Fe atoms. By a combination of both radiations, more precise results were obtained in comparison to the individual refinements. The FULLPROF program was employed to carry out these joint refinement with the same profile settings as used in separate refinements. Obtained occupation factors for *B*-site cations were then fixed and used further in all refinements of NPD patterns at low and high temperatures.

2.6 Theoretical modelling

In order to clarify the influence of Sc doping on structural and magnetic properties of PFSWO theoretical investigations were performed. First-principles density functional theory (DFT) calculations were performed using the VASP package [55] based on plane wave basis set and projector augmented wave method [56]. For the treatment of exchange-correlation, Perdew-Burke-Ernzerhof [57] generalized gradient approximation (GGA) has been considered. In order to include strong electron correlations, a static mean-field approach (GGA+U) [58] commonly used to describe the electronic structures of correlated oxides [59] was employed. We have considered the U value of 4 eV for the Fe-d electrons [60] while the exchange interaction J_H was kept as 0.9 eV. The geometries were relaxed until the forces on all atoms were reduced to 15 meV/Å. A plane-wave energy cut-off of 400 eV was used, and a $10 \times 10 \times 3$ Monkhorst-Pack k-points mesh was used for Brillouin zone integration for the geometry relaxations and a $15 \times 15 \times 5$ k-points mesh for the calculations of the total energies. Regarding the magnetic structures, we have considered both ferromagnetic (FM) and antiferromagnetic (AFM) alignment of Fe moments. For AFM structures, we considered magnetic structures close to G-type as much as possible.

3 Results

3.1 Sample characterization

After multiple grinding and heating cycles, the XRPD patterns collected from the PFSWO solid solutions were invariant, indicating that no further reaction was occurring. From inspection of these patterns, it was evident that there are three ranges in this composition series of compounds: single phase samples were obtained at each end of the compositional series and a two-phase region exists between them. Multiple attempts were made to convert two-phase samples into single phases, with repeated synthesis, alterations of heating temperature and rapid cooling but in most of the cases, two-phase samples resulted. Only the above-indicated quenching procedures provide single phase PFSWO samples. The lattice constant increases for higher Sc content. This behaviour can be correlated to a greater radius of Sc^{3+} (0.745 Å), as compared to that of Fe^{3+} (0.64 Å) [61]. For a given composition, the volume of the cells generally decreases with increasing sintering time. This could be due to improved cationic order and a decreasing number of antisites.

3.1.1 Annealed samples

The position and intensities of the reflections in the XRPD patterns of the annealed samples were consistent with those expected for PFWO and PFSWO-based solid solutions with cubic perovskite structure [41,42,47]. Reflections from secondary phases were not detected in the XRPD patterns. Structural refinement studies of the annealed XRPD powder diffraction patterns of PFSWO with $x < 0.05$ confirm that these samples stabilize in cubic $Pm\bar{3}m$ symmetry at room temperature, which is in accordance with earlier studies [47]. For samples with $0.05 \leq x \leq 1$, a set of additional superstructure reflections was found and the crystal structure of PFSWO stabilizes in cubic $Fm\bar{3}m$ symmetry, with the cell doubled in all directions in comparison to that of the $Pm\bar{3}m$ structure. Thus, the addition of more than 5 at.% Sc to PFWO leads to *B*-site cation ordering (introduction of

Table 1. Results of Rietveld refinements of XRPD patterns for annealed $Pb(Fe_{1-x}Sc_x)_{2/3}W_{1/3}O_3$ samples ($0.1 < x < 0.4$).

x	Phase 1 $Pm\bar{3}m$ a (Å)	Phase 2 $Fm\bar{3}m$ a (Å)	Phase composition $Pm\bar{3}m/Fm\bar{3}m$ (%)	R_p, R_{wp}, R_{B1}, R_{B2}
0.1	3.9837(6)	3.9794(6)×2	34.8/65.2 (0.3)	5.63, 7.31, 5.09, 6.67
0.2	3.9986(5)	3.9883(5)×2	26.6/73.4 (0.3)	5.14, 7.06, 4.78, 6.83
0.3	4.0019(5)	3.9904(5)×2	21.4/78.6 (0.3)	5.25, 7.17, 4.91, 7.03
0.4	4.0093(6)	4.0011(6)×2	15.8/84.2 (0.3)	4.96, 6.98, 5.01, 7.11

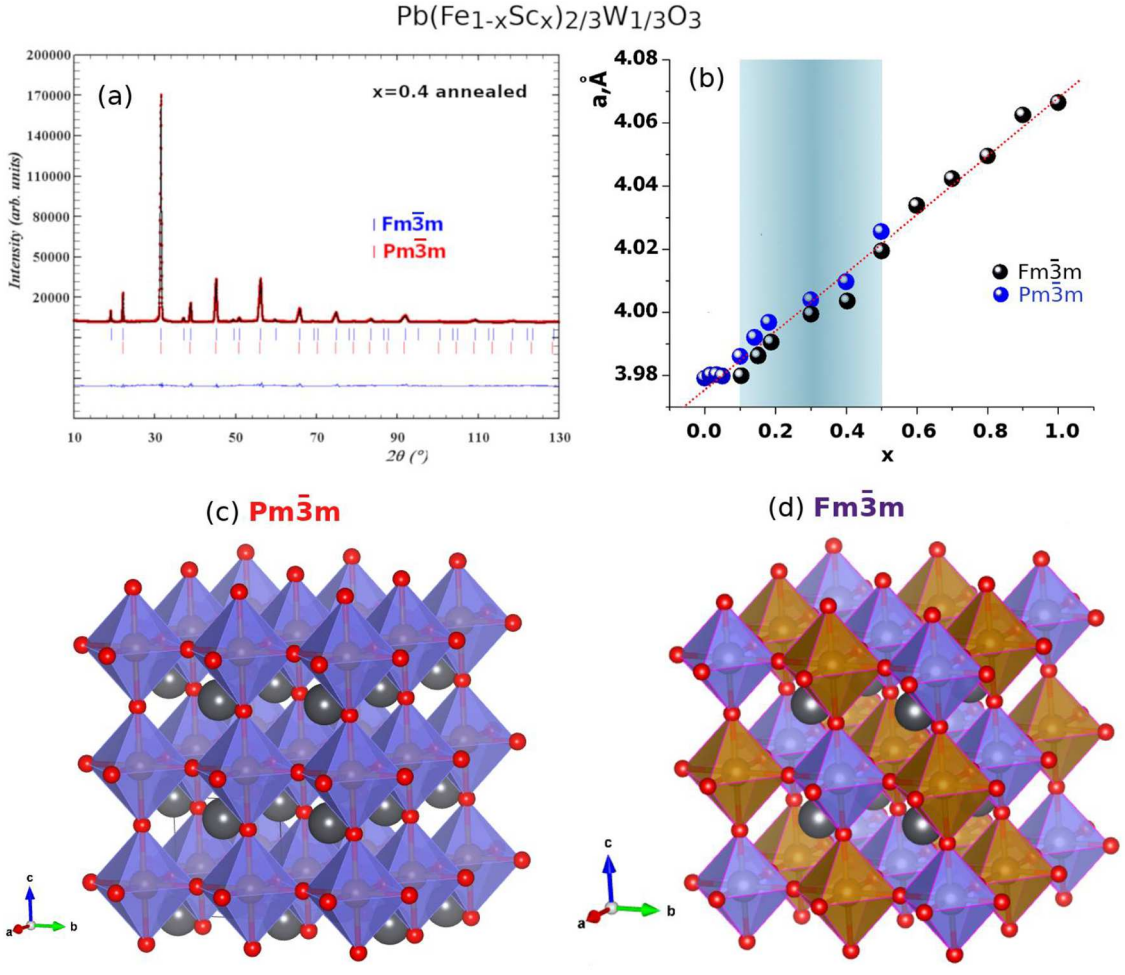

Fig. 1. (a) Two-phase refined XRPD pattern for the annealed $Pb(Fe_{1-x}Sc_x)_{2/3}W_{1/3}O_3$ sample with $x = 0.4$, illustrating the respective reflections from $Pm\bar{3}m$ and $Fm\bar{3}m$ phases (see Tab. 1 for phase composition). (b) Lattice parameters observed from XRPD data as a function of Sc concentration x for annealed $Pb(Fe_{1-x}Sc_x)_{2/3}W_{1/3}O_3$ samples; the $Fm\bar{3}m$ lattice parameter is plotted as a ($Fm\bar{3}m$)/2. (b) schematic phase diagram (c,d): polyhedral representations of the crystal structures, drawn using VESTA [62]; Pb ions are drawn in grey, oxygen anions in red, and the Fe(W)O_6 and Fe(Sc)O_6 octahedra in violet and orange respectively.

two independent B-sites). As the Sc content increases, the relative intensity of the superlattice reflections progressively increases. For PFSWO with x between 0.1 and 0.4 the main peaks are split, which reflects the formation of two cubic perovskite phases: a major phase of symmetry $Fm\bar{3}m$ and a minor phase of symmetry $Pm\bar{3}m$. This conclusion is consistent with earlier work [41,42] where all PFSWO samples contained a mixture of phases. As the value of x is increased, the magnitude of the peak splitting diminishes and the relative intensity of the peaks at lower angle decreases, implying that the relative amount of the $Pm\bar{3}m$ perovskite phase decreases; e.g. from about 30% for $x = 0.2$ to 15% of sample weight for $x = 0.4$ (see Tab. 1). Figure 1 shows the evolution of the lattice parameter and the structure of PFSWO with Sc content. In Figure 1b, the lattice parameter of the $Pm\bar{3}m$ and $Fm\bar{3}m$

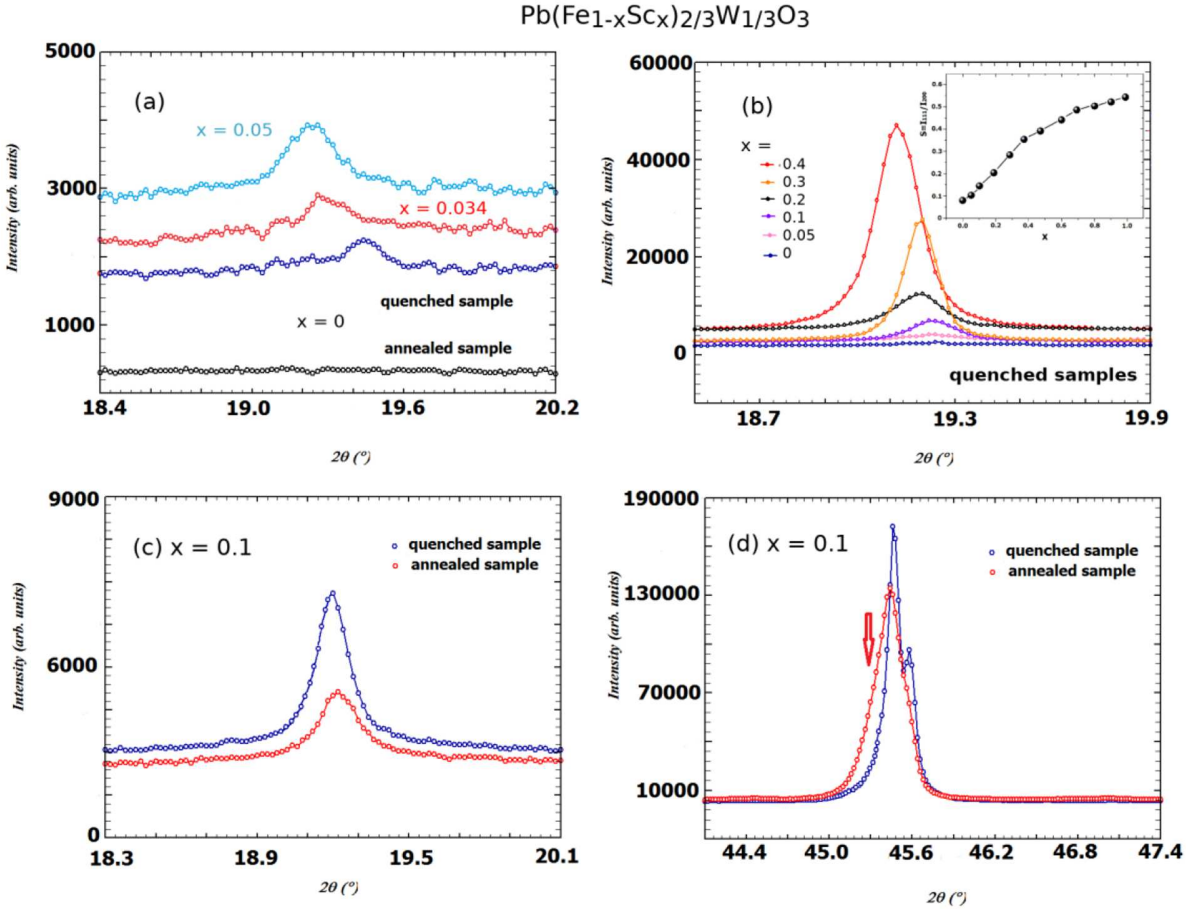

Fig. 2. XRPD patterns of the annealed and quenched $Pb(Fe_{1-x}Sc_x)_{2/3}W_{1/3}O_3$ samples for (a) low Sc concentrations, (b) $0 \leq x \leq 0.4$ (quenched samples only), and (c,d) $x = 0.1$. The inset in (b) shows the evolution of the order parameter S for the quenched samples.

phases are plotted including the behaviour in the two phase region, where the lattice parameter of the ordered $Fm\bar{3}m$ phase is slightly smaller than that of the $Pm\bar{3}m$ phase. Figures 1c and 1d show schematic representations of the structures illustrating the difference between the $Pm\bar{3}m$ and $Fm\bar{3}m$ cubic phases. At low temperatures in the composition range $x = 0.1{-}0.5$, there is a dissolution gap, which is absent at high temperatures where an unlimited series of solid solutions is formed in the system (see Fig. SM1 in the Supplemental Materials for a schematic illustration of the phase diagram of the solid solution system).

3.1.2 Quenched samples

XRPD-based phase analyses of PFSWO samples obtained by quenching after prolonged calcination at 840 °C (76 h) showed that single-phase solid solutions with $Fm\bar{3}m$ structure are formed throughout the composition range. This difference between quenched and annealed samples is exemplified in Figure 2. In e.g. Figure 2d which shows parts of the XRPD patterns taken on two $x = 0.1$ samples; a splitted peak is observed for the quenched sample. Figure 2b illustrates the enhancement of the peak for quenched samples with increasing x. The degree of chemical B-site ordering (S) reflecting the occupation of the two independent B-sites was determined for quenched samples using room temperature XRPD patterns and is plotted vs. x in Figure 2b. S is evaluated from the ratio of the observed superlattice reflection (111) to the nearest base lattice reflection (200) using the equation $S = (I_{111}/I_{200})$ (see details in [63,64]).

After contrasting the structural properties of the annealed and quenched samples, only the structural, dielectric, and magnetic properties of the quenched samples are investigated in detail below.

3.2 Chemical composition

The ceramic samples of PFSWO were obtained with a density reaching 90–93% of the theoretical one. The density of the samples decreased with increasing Sc content. At the maximum firing temperatures, thermogravimetric curves showed weight losses that varied between 0.5 and 0.7% for all samples, indicating that they possess good thermal stability in air and that their overall oxygen stoichiometry is nearly constant under temperature variation. SEM with EDS point analyses of different grains were recorded for samples with $x = 0.1$, 0.2, 0.3, and

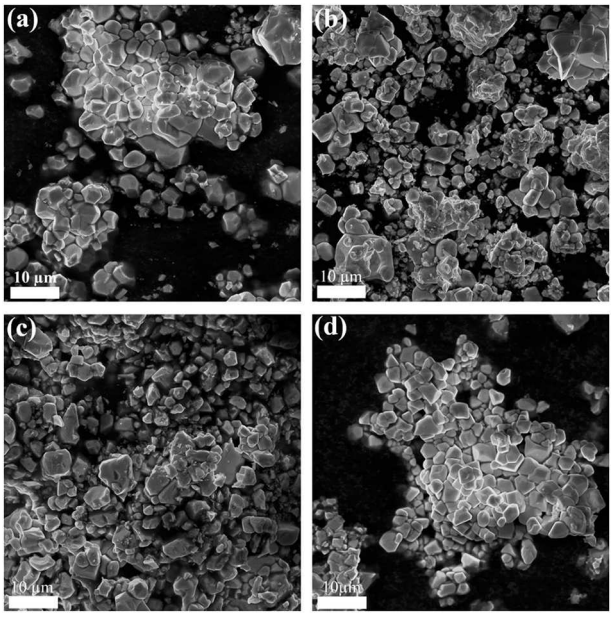

Fig. 3. SEM images of the quenched $Pb(Fe_{1-x}Sc_x)_{2/3}W_{1/3}O_3$ samples with (a) $x = 0.1$, (b) $x = 0.2$, (c) $x = 0.3$, and (d) $x = 0.4$.

0.4. From analyses of the images exemplified in Figure 3, it is found that the Sc/(Fe + Sc) ratio and Pb contents are close to their nominal values. The variation in the Sc/(Fe + Sc) ratio is largest (but still close to the nominal value) between different grains for $x = 0.2$. For $x = 0.3$, the Pb content is slightly less than the nominal value. Based on 130–160 measured points for each x, it was established that the Sc and Fe content for all x-values are close to the nominal values within the standard deviation. In addition, the Pb and W content is on average close to the nominal value, however, with a standard deviation that appears to increase with increasing x. For the $x = 0.4$ sample, the average values of the metal ion contents deviate most from the nominal values, since a few grains of higher Fe content are observed.

In general, the particle size in the samples varies between 1 and 7 μm for all x-values. However, it appears that the average grain size decreases with increasing x since the amount of small grains, $<2\,\mu$m, increases with increasing x shifting the median grain size towards 1–3 μm. As all the samples were prepared under the same conditions, this difference in microstructure can be attributed to effects of the Sc^{3+} ions. The grain growth in solid state synthesis is strongly dependent upon the rates of diffusion. The higher melting point of Sc_2O_3 (2485 °C) than Fe_2O_3 (1565 °C) and WO_3 (1473 °C) suggests that the diffusion of Sc is slower than that of Fe and W during the synthesis process and hence may cause the smaller grain sizes of samples having higher Sc contents.

The EDS elemental analyses of the quenched PFSWO samples used in XRPD and magnetic measurements detected only Pb, Fe, Sc and W cations. The averaged ratios between each element and the sum of elements (Pb + Fe + Sc + W) obtained by EDS and calculated according to the nominal composition are found to agree within the accuracy of the EDS analyses. The EDS study of an undoped sample confirmed a cationic ratio of Pb:Fe:W of 3:2:1, in agreement with the nominal one. Complementary ICP composition analyses also indicate that the ratios of Pb:Fe:Sc:W were in agreement with the nominal values. Mössbauer spectroscopy results show that the Fe ions in PFSWO reside in the high spin Fe^{3+} state and occupy inequivalent positions differing in the nearest cation environment [47,54].

3.3 Dielectric properties

The temperature dependences of the relative dielectric permittivity $\varepsilon(T)$ and dielectric loss tangent $\tan\delta(T)$ for annealed samples have prominent, broad maxima in the range 180–250 K, whose position (T_{max}) shifts to higher temperatures with increasing frequency (see Fig. SM2). Such behaviour is characteristic of ferroelectric relaxors, which include PFWO [9,10,13] and PSWO [65–67]. The temperature-frequency dependence of the dielectric constant ϵ and losses $\mathrm{tg}\delta$ of quenched samples of PFSWO are qualitatively similar to that of the annealed samples, as illustrated in Figure 4 for the samples with $x = 0.1$ and $x = 0.4$. They also exhibit pronounced wide permittivity maxima characteristic for ferroelectric relaxors, the positions of which are shifted with frequency toward higher temperatures. At the same time, the position of these peaks on the temperature scale practically corresponds to the position of the peaks of the slowly cooled samples, but the magnitude of the peaks of the quenched samples increases approximately by a factor of 2 (see Fig. SM2). One puzzling point in the structural interpretation of the dielectric relaxation is the fact that the observation of partial order in PFSWO does not result in the disappearance of this relaxation. Indeed, when increasing the Sc content in PFSWO solid solutions, the dielectric relaxation is observed up to 100% content of Sc. Dielectric hysteresis loops were experimentally measured at room temperature using a Sawyer-Tower circuit at the frequency of 50 Hz. As seen in Figure 5, the obtained dielectric loops resemble those of linear lossy dielectrics. No saturation can be observed while increasing the amplitude of the electric field E. Increasing E above 12 kV/cm for $x = 0.1$ and above 7 kV/cm for $x = 0.4$ caused the breakdown of the samples. The absence of saturation is probably due to the cubic symmetry of the studied solid solutions and the low amplitudes of the applied ac electric fields. The observed relatively low breakdown voltages are due to the rather high conductivity of the samples.

3.4 Magnetization studies

The zero field cooled (ZFC) and field cooled (FC) temperature dependence of the magnetization M(T) in the temperature interval $T = 5$–400 K is shown in Figure 6. To record the ZFC magnetization, the sample was first cooled to a low temperature in the absence of a magnetic field where the magnetic field was applied and the ZFC magnetization recorded on warming the sample. The FC data was recorded on warming, after cooling the sample in a magnetic field. As the temperature decreases from

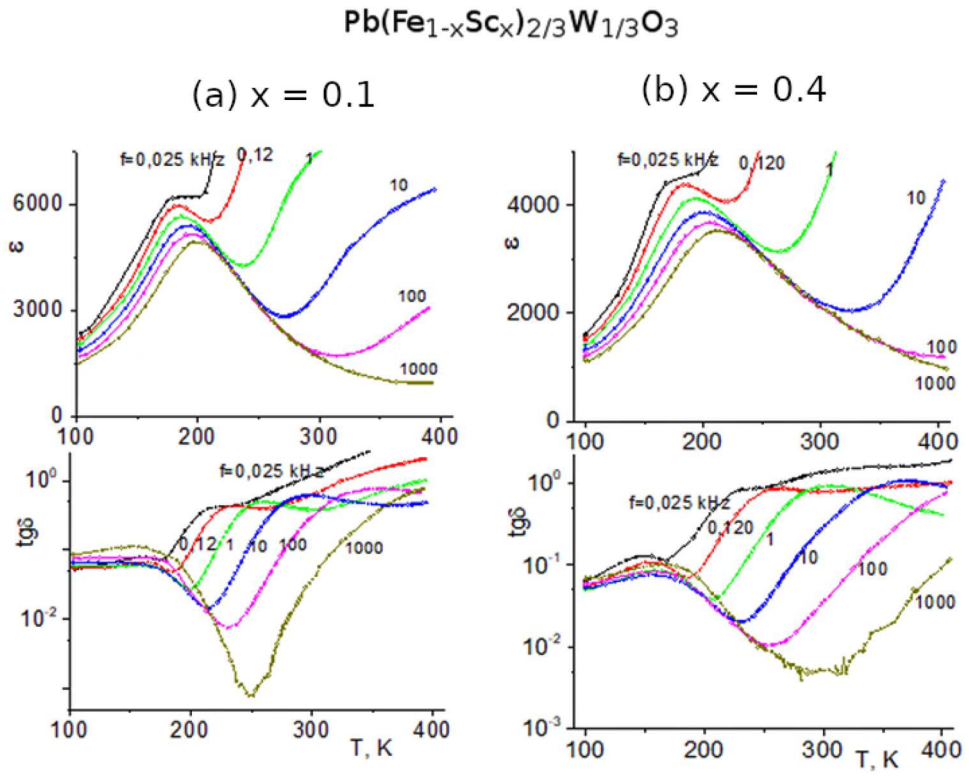

Fig. 4. Temperature dependence of the dielectric properties of the quenched $Pb(Fe_{1-x}Sc_x)_{2/3}W_{1/3}O_3$ samples with (a) $x = 0.1$ and (b) 0.4.

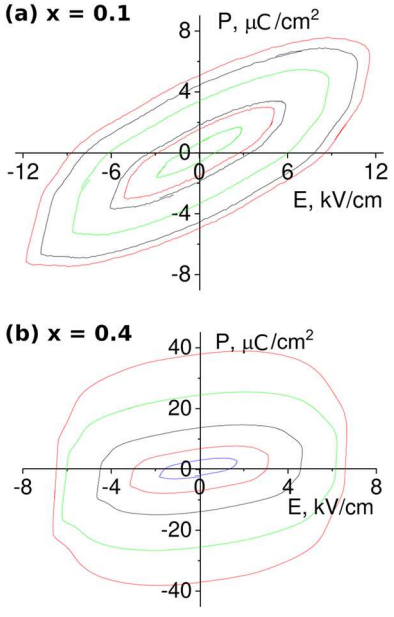

Fig. 5. Room-temperature dielectric hysteresis loops of the quenched $Pb(Fe_{1-x}Sc_x)_{2/3}W_{1/3}O_3$ samples with (a) $x = 0.1$ and (b) 0.4. E is the applied electric field, and P the electric polarization.

400 K, all samples exhibit an anomaly at a characteristic temperature that decreases with increase in the value of x (shown by arrows in Fig. 6). These anomalies are representative of the magnetic ordering temperatures of the samples, and occur at $T > 200$ K for the low doped samples ($x = 0.1$ and 0.2), and at $T < 200$ K for higher values of x ($x = 0.3$ and 0.4). The value of the magnetization varies non-linearly with x. This non-linearity is independent of the measuring field or the measurement protocol used (i.e., the same non-linearity is observed in data extracted from magnetization versus temperature measurements as well as from magnetization versus magnetic field measurements). This can be observed in Figure 7a, where we show the ZFC and FC magnetization versus temperature curves of the samples recorded under a lower magnetic field $H = 0.01$ T (main panel). The observed magnetic irreversibility in the magnetization data depicted in Figure 7a may stem from the temperature-dependent coercivity of the excess moment induced in the materials [35].

The isothermal magnetization curves recorded at $T = 5$ K are shown in Figure 7b. The M vs H curves exhibit open loops near the origin (inset of Fig. 7), indicating the presence of uncompensated magnetic moments in all the samples. The coercive field varies between $H_C = 0.035$–0.05 T for different values of x. The high field data shows an absence of magnetic saturation, consistent with the ferrimagnetic nature of the samples. The ferrimagnetic transition temperature of PFSWO decreases with increasing x, due to the magnetic dilution of the B sites with diamagnetic Sc. The decrease occurs in a similar way for quenched and annealed samples However, as illustrated in Figure SM3 for the sample with $x = 0.2$, the excess moment is significantly higher for the quenched samples.

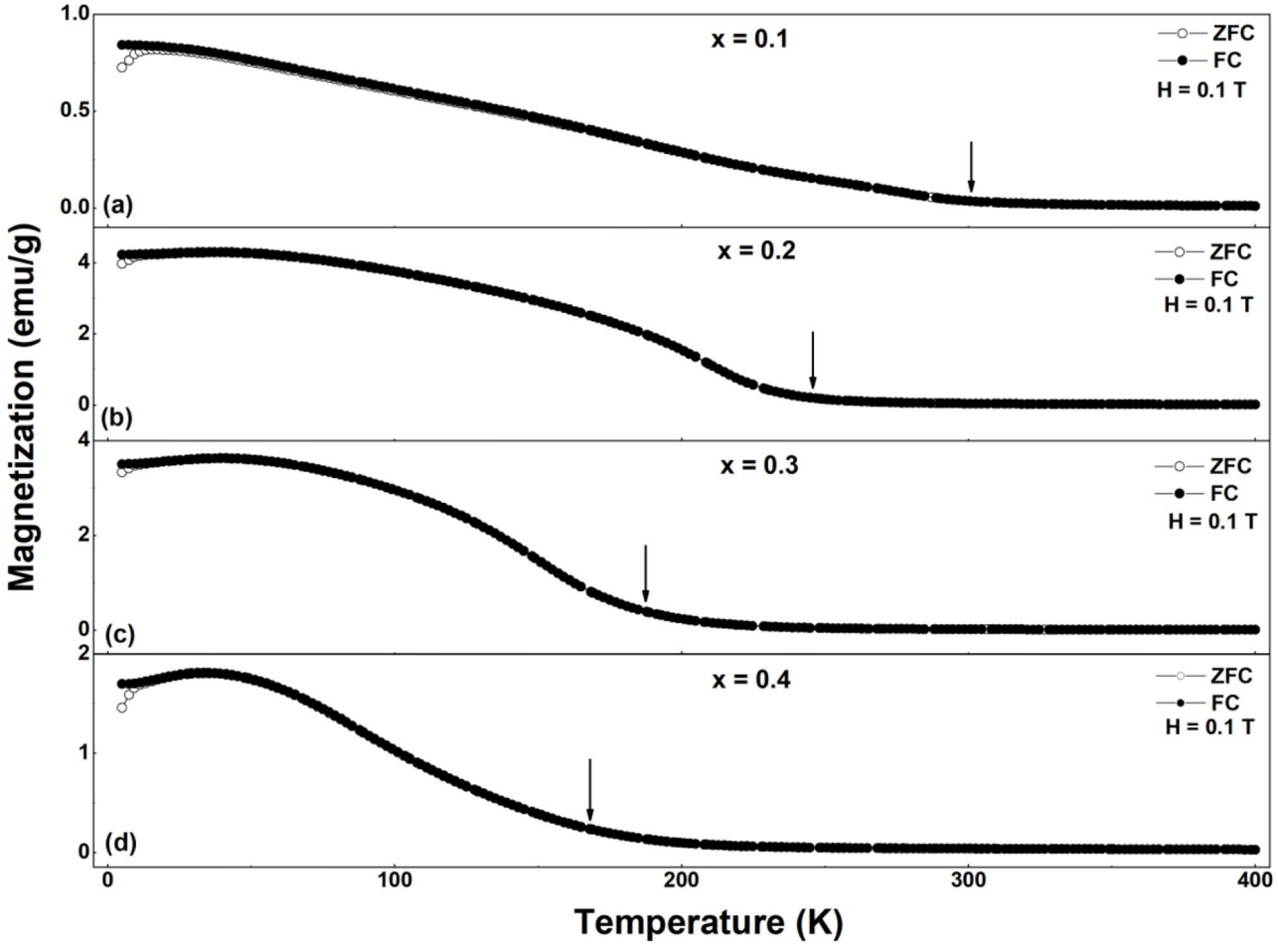

Fig. 6. ZFC/FC magnetization curves of the quenched $Pb(Fe_{1-x}Sc_x)_{2/3}W_{1/3}O_3$ samples ($0.1 \leq x \leq 0.4$); $H = 1$ kOe. Arrows indicate the onset of magnetic ordering of the materials.

3.5 NPD and SXRPD studies

The structural refinements of NPD data sets measured on the quenched $x = 0.1$, 0.2, 0.3, and 0.4 samples were performed in the $Fm\bar{3}m$ space group (No. 225). Figure 8 shows measured and refined NPD patterns for the $x = 0.1$ and $x = 0.4$ samples at 4 K. The intensity colour maps of the low-angle part of the NPD patterns plotted in Figures SM6 and SM7 show the evolution of the intensity of the (111) and (002) reflections with the temperature and x. The Fe, Sc, and W atoms are located at the *4a*(0,0,0) and *4b*(1/2,0,0) crystallographic Wyckoff sites. The O atoms are found at the *24e* site (x,0,0), the x coordinate takes the value of 0.25 for an ideal primitive cubic cell and its deviation from 0.25 determines the difference between B'–O and B''–O distances. Finally, the Pb atoms occupy the *8c*(1/4,1/4,1/4) sites. It should be noted that the $Fm\bar{3}m$ space group does not allow any tilt or rotation of the *B*O6 octahedra nor polyhedral distortions; however, different *B*–O bond distances between two sites are permitted, owing to oxygen displacements along the x-axis. It is noteworthy that a local distortion of the Pb environment was detected. When refinements are carried out with the Pb atom fixed at the high symmetry (1/4, 1/4, 1/4) site, anomalously large isotropic displacement parameters, suggesting static disorder, are observed. In order to retain the cubic symmetry, split positions were adopted for Pb. In contrast, Fe (Sc,W) and oxygen were left at their special sites, after verification that their displacements did not improve the refinement. The structure was very well refined as cubic disordered, with disorder confined only at the Pb site. Bond valence calculation on both the *A*- and *B*-site show very good agreement with the expected oxidation state of the ions – Pb^{2+}, Fe^{3+}, Sc^{3+} and W^{6+}.

Figure 9 shows the measured and refined diffraction patterns of NPD (Fig. 9a) and SXRPD (Fig. 9b) for the $x = 0.3$ sample at room temperature, used for the joint refinement. The distribution of the three different transition metal cations on the two available *B* sites has been refined assuming the nominal Fe:Sc:W ratio and using the determined ratio of (Fe + Sc)/W on the two sites from the joint refinement of SXRPD and NPD data. In fact Fe and Sc are, due to their nearly identical scattering form factors, nearly indistinguishable in X-ray scattering while the contrast to W is strong. The neutron scattering signal from Sc and Fe however dominates over that of W. The refinements indicate an increase of the degree of cation site order as the Sc content increases.

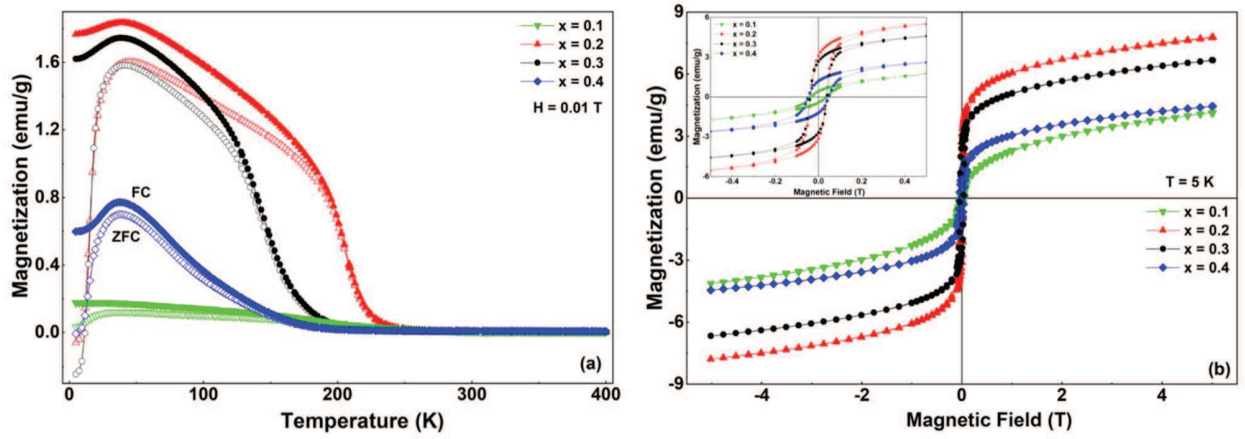

Fig. 7. (a) ZFC/FC curves magnetization curves of the quenched $Pb(Fe_{1-x}Sc_x)_{2/3}W_{1/3}O_3$ samples ($0.1 \leq x \leq 0.4$); $H = 100$ Oe. (b) Isothermal magnetization vs magnetic field $M(H)$ curves at $T = 5$ K for the same materials; inset shows a closer view of the low-magnetic field region.

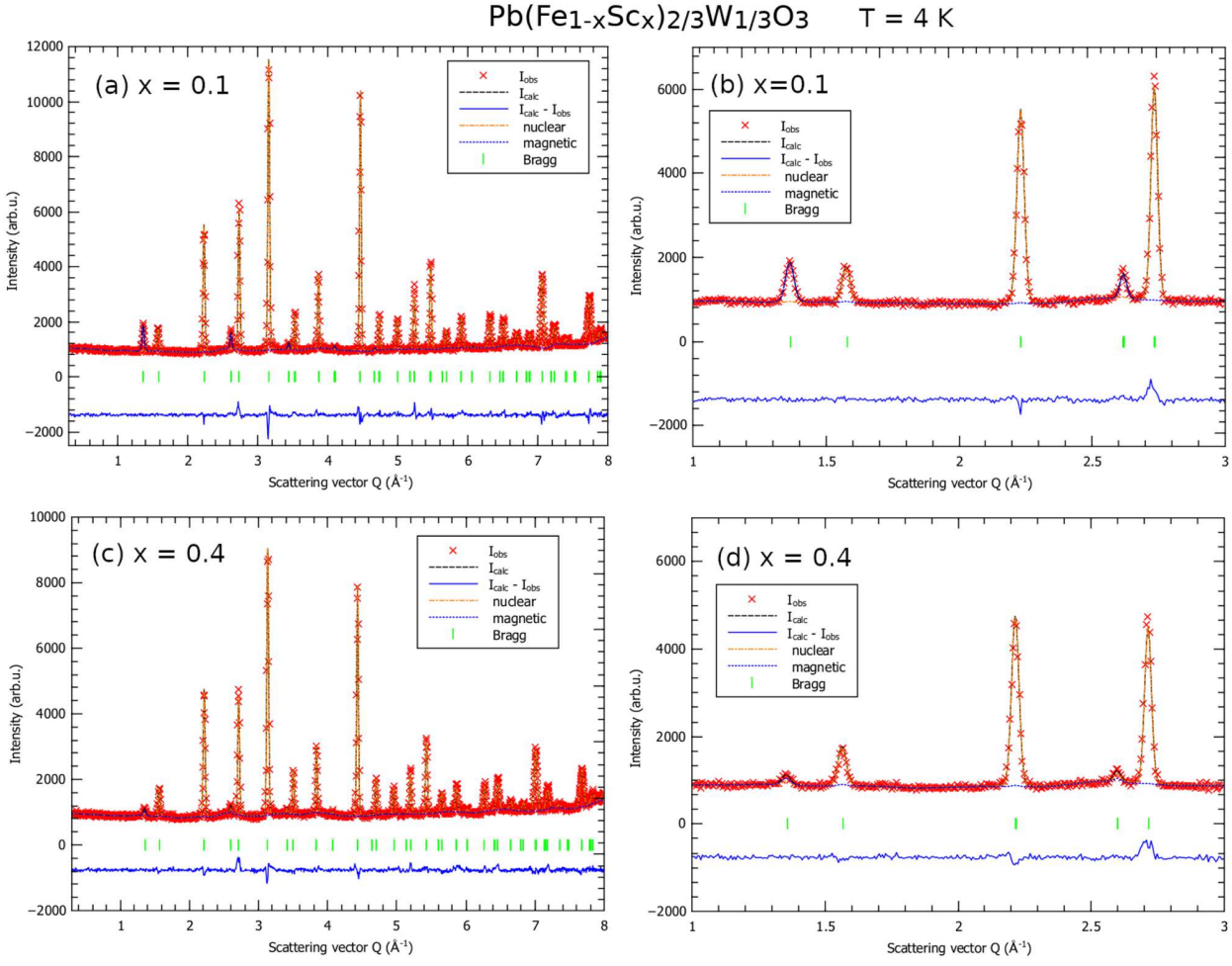

Fig. 8. Refinements of the NPD data at $T = 4$ K for (a,b) $x = 0.1$ (Refinement quality factors: R_B: 3.80, R_p: 3.36, R_{wp}: 4.34) and (c,d) $x = 0.4$ (R_B: 4.65, R_p: 3.15, R_{wp}: 4.04). Panels (b) and (d) are detail views of panels (a) and (c), respectively.

The lattice parameters (Fig. SM4), B–O bond distances (Fig. SM5) and *B*-site occupancies (Fig. 10) were derived from the joint SXRPD + NPD data. The Fe(Sc):W ratio was constrained to 2:1 in all refinements although the distribution of the cations over the two crystallographically-distinct sites was allowed to vary. Both Fe and W cations were found to be present on both *B* sites in PFSWO. The Fe:Sc:W distributions deduced

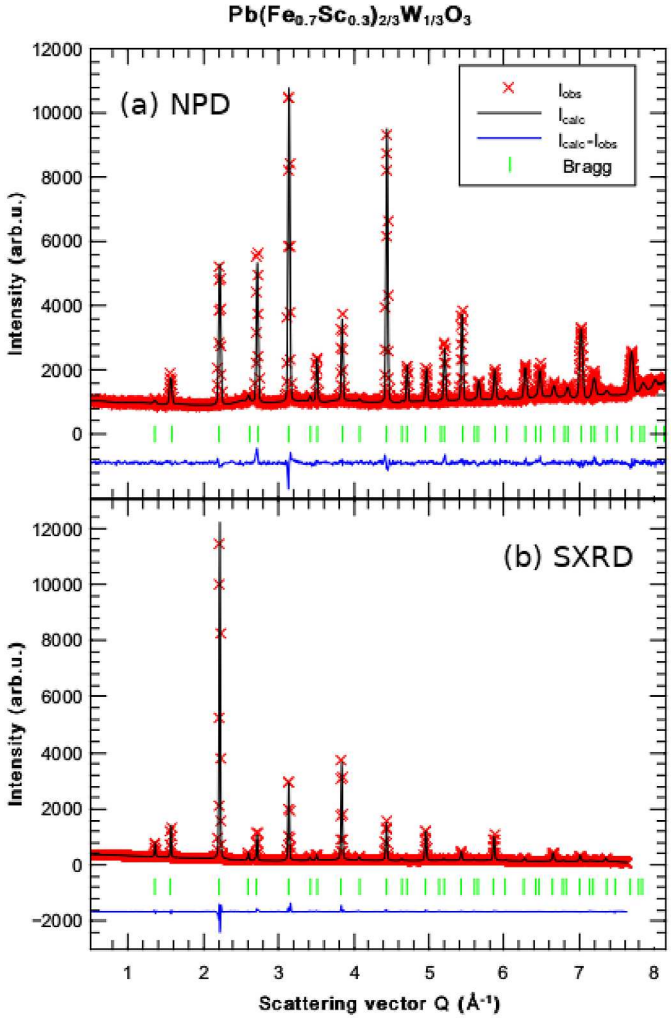

Fig. 9. Results of joint NPD + SXRPD refinements for the quenched $Pb(Fe_{1-x}Sc_x)_{2/3}W_{1/3}O_3$ sample with $x = 0.3$; $T = 295$ K (NPD: R_B: 4.40, R_p: 2.94, R_{wp}: 3.77; SXRPD: R_B: 3.73, R_p: 2.76, R_{wp}: 5.10).

from the data collected at room temperature were held fixed during the analyses of the NPD datasets collected at 4 K. It is well known [68] that determination of the distribution of three different kinds of atoms (Fe, Sc, W) on two available crystallographic sites (*4a* and *4b* in $Fm\bar{3}m$) requires at least two sets of diffraction data with differing atomic cross sections, but even then is nontrivial by Rietveld refinement. However, using combined refinements, conclusive results about the cation distribution were obtained.

3.6 Theoretical results

It is known from our experiment that Sc replaces Fe in the *B* sublattice with W sites remaining almost unaffected. Therefore, in all calculations, we have replaced Fe only by Sc. Several concentrations of Sc were considered initially (up to $x = 0.25$) with many configurations per concentration (not shown here) to check the tendency of Sc site occupation. Our initial finding suggested that clustering of Sc is not favorable. Our experiments suggested the ordering of Sc atoms after substitution. This ordering tendency increases with increasing Sc concentration. In order to know whether the Sc atoms are more likely to be periodically distributed in the structure for high Sc concentration, we considered structural models with the periodic and non-periodic arrangement of Sc atoms for two different concentrations: $Pb_{12}Fe_6Sc_2W_4O_{36}$ (0.25) and $Pb_{12}Fe_5Sc_3W_4O_{36}$ (0.375) as shown in Figure 11. The supercells were built up with six octahedra along the *c*-axis (Figs. 11b and 11c) and $\sqrt{2}a \times \sqrt{2}a$ in plane geometry.

In Table 2, we show the relative energies of FM and AFM alignments of Fe moments along with local moments on Fe averaged over all Fe sites. Two concentrations of Sc have been shown.

The first observation is that for all concentrations, the ground state tends to be the G-type AFM structure with Sc atoms arranged in an ordered fashion. This is in agreement with the experimental finding. For $Pb_{12}Fe_6Sc_2W_4O_{36}$ ($x = 0.25$), the lowest energy structure is periodic AFM, and second lowest energy structure is non-periodic AFM; the energy difference between these two states is 0.28 eV. For $Pb_{12}Fe_5Sc_3W_4O_{36}$, the minimum energy structures are periodic; the energy of the AFM state is 0.17 eV lower than the FM state, and the energy difference between the periodic and non-periodic configurations is approximately 1 eV. As with increasing Sc concentration, Fe atoms are on the average, more distant apart, the strength of exchange interaction decreases. According to Goodenough-Kanamori rules [69,70], a 180° superexchange (the magnetic ion-ligand-magnetic ion angle is 180°) between two magnetic ions with partially filled d shells is strongly antiferromagnetic. In low Fe concentration structures, the impact of the superexchange effect is very small.

We also compared the volume change of the octahedra in the system before and after doping. According to our results, after Sc doping, the volume of PFWO increases, and the FeO_6 octahedra are more prone to changes than WO_6 octahedra. For $x = 0.25$, the average volume changes in these two octahedra are 0.13 Å^3 and 0.09 Å^3, respectively.

3.7 Magnetic structure determination

There is no evidence of structural phase transition upon cooling from neutron diffraction patterns. The nuclear structure can be described by $Fm\bar{3}m$ model down to 4 K. Increase of the intensity of certain Bragg reflections below the magnetic transition indicates that the magnetic unit cell is the same as the nuclear one. The symmetry analyses of possible spin arrangements were performed using BASIREPS software [47] as well as Bilbao Crystallographic Server (BCS) [53]. The BASIREPS software reveals only one possible spin arrangement Γ9 (s.g.F-1), where the spins can have components along all three orientations, which can be refined independently. Refinements using three independent components were unstable. The BCS results revealed more suitable options with several partial decreases of symmetry leading to the subgroups of $Fm\bar{3}m$. After refinement of all relevant models

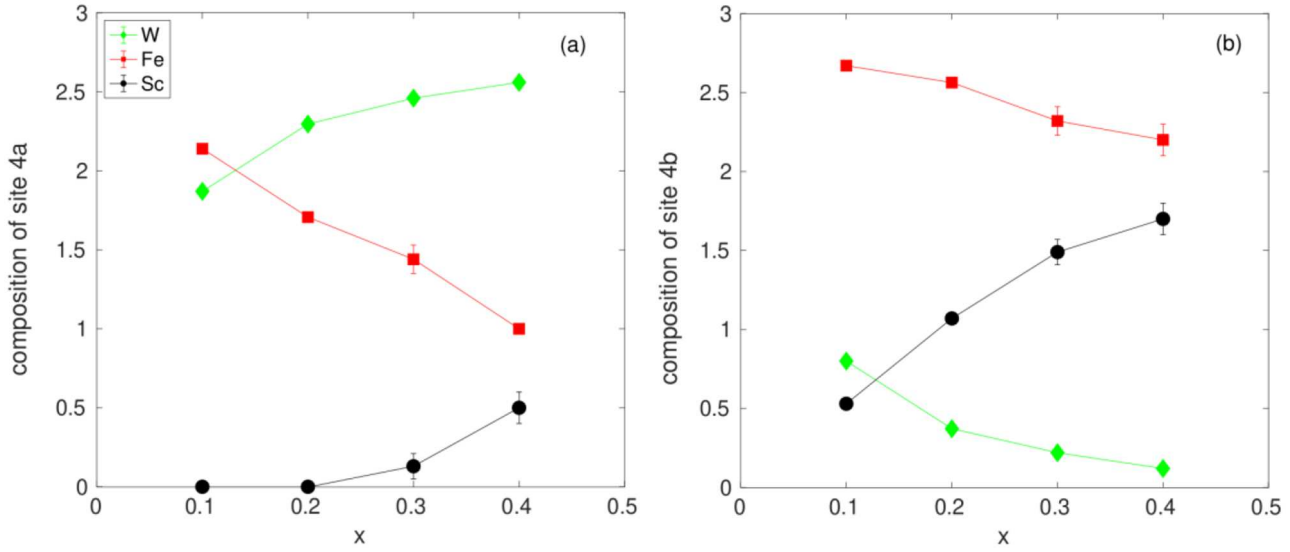

Fig. 10. (a) *4a*- and (b) *4b*-site occupancy of the Fe, W, and Sc cations extracted from NPD + SXPRD for the quenched $Pb(Fe_{1-x}Sc_x)_{2/3}W_{1/3}O_3$ samples ($0.1 \leq x \leq 0.4$). Total occupancy is 4 per *4a*/*4b*-site.

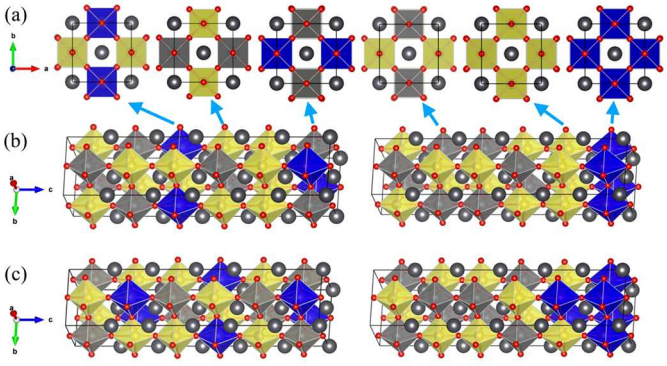

Fig. 11. (left) Periodic and (right) non-periodic clustered structures of $Pb(Fe_{1-x}Sc_x)_{2/3}W_{1/3}O_3$ for (a) and (b) $x = 0.25$ and (c) $x = 0.375$. The O atoms are shown by red spheres, the Pb atoms are by black. The FeO_6 octahedra are highlighted with light yellow color, the WO_6 octahedra with grey, and the ScO_6 with blue. (a) Shows the top view of specific ab planes indicated by arrows in (b), both of which representing the structural models for $x = 0.25$.

against the neutron diffraction pattern collected at 4 K, the two models with magnetic space groups $I4/mm'm'$ (BNS: 139.537) and $R\bar{3}m'$ (BNS: 166.101) were found to fit the measured intensities. Both models give exactly the same R-factors, so the models cannot be distinguished by the means of the powder diffraction. The tetragonal model ($I4/mm'm'$) has the spins arranged antiferromagnetically along the z-axis. The rhombohedral model ($R\bar{3}m'$) has the same antiferromagnetic arrangement but the spins are canted in the ⟨111⟩ direction. During the refinement, all structural parameters were constrained to maintain the cubic symmetry of the nuclear phase and decrease of the symmetry is related only to the spin arrangement.

Figure 12 shows schematic representations of the magnetic arrangement in the $R\bar{3}m'$ and $I4/mm'm'$ models. In the final stage of the refinements, it was possible to determine the magnetic moments of the two different magnetic sites restrained to the same ratio as occupation factor.

The total magnetic moment of the unit cell is zero in the ideal AFM structure but in the case of PFSWO the two magnetic sub-lattices are not equivalent and non-compensated. The thermal variation of the magnetic moment for the different PFSWO compositions is plotted in Figure 13. The disappearance of the magnetic moments at higher temperatures for the different samples accord with the decay of the magnetic transition temperatures derived from the magnetisation measurements. In Figure 14a, the magnetic moments estimated for the *4a* and *4b* from the NPD experiments are plotted as a function of Sc concentration. An uncompensated magnetic moment may be estimated from the difference between the two magnetic moment values. As seen in the figure, this difference amounts to approximately 1 μ_B per pair of *B*-sites, which is comparable in magnitude with the magnetization at high magnetic field and low temperature M(H = 50 kOe, $T = 5$ K) extracted from the magnetization measurements plotted in Figure 14b (extracted from the plots shown in Fig. 7b). It is also clear from Figure 13a that the dilution of the *B* sublattice with Sc produces a decrease in the average moment. However, the local moment of the Fe^{3+} cations does not change appreciably and remains close to 5 μ_B ($\times 2/3 \sim 3.35\,\mu_B$) (in calculations the local moment of Fe is found to be approximately 4.2 μ_B, see Tab. 2).

Most remarkably, the NPD data of a pure PFWO sample quenched in the same conditions as the doped ones indicates partial ordering of the *B*-site; see Fig. 15a), where an NPD pattern of a quenched PFWO sample is shown. Refinements of the NPD patterns for this quenched PFWO sample yields a temperature dependence of the magnetic moments on the *B*-sites as shown in Figure 15b (data was collected at 325 K and above). There is a large

Table 2. Relative energies E (in eV) and average Fe magnetic moments μFe (in μ_B) for each structure. For each concentration, the lowest energy is set to be zero.

	Periodic				Non-periodic			
	FM		AFM		FM		AFM	
	E	μFe	E	μFe	E	μFe	E	μFe
$x = 0.250$	0.43	4.21	0.00	4.12	1.79	4.02	0.28	4.12
$x = 0.375$	0.17	4.18	0.00	4.20	1.04	4.16	1.06	3.88

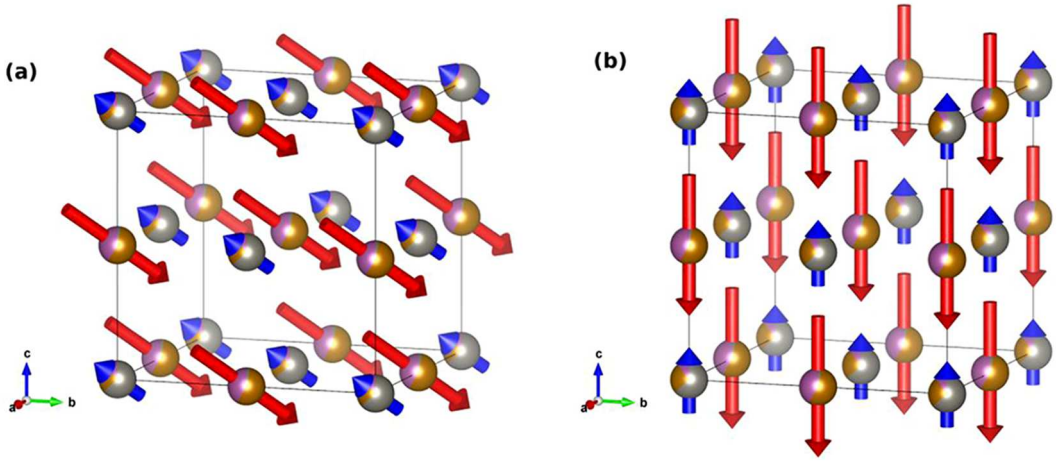

Fig. 12. Ferrimagnetic magnetic structure determined from the NPD data: (a) rhombohedral model ($R\bar{3}m'$) and (b) tetragonal model ($I4/mm'm'$); drawn using VESTA [62].

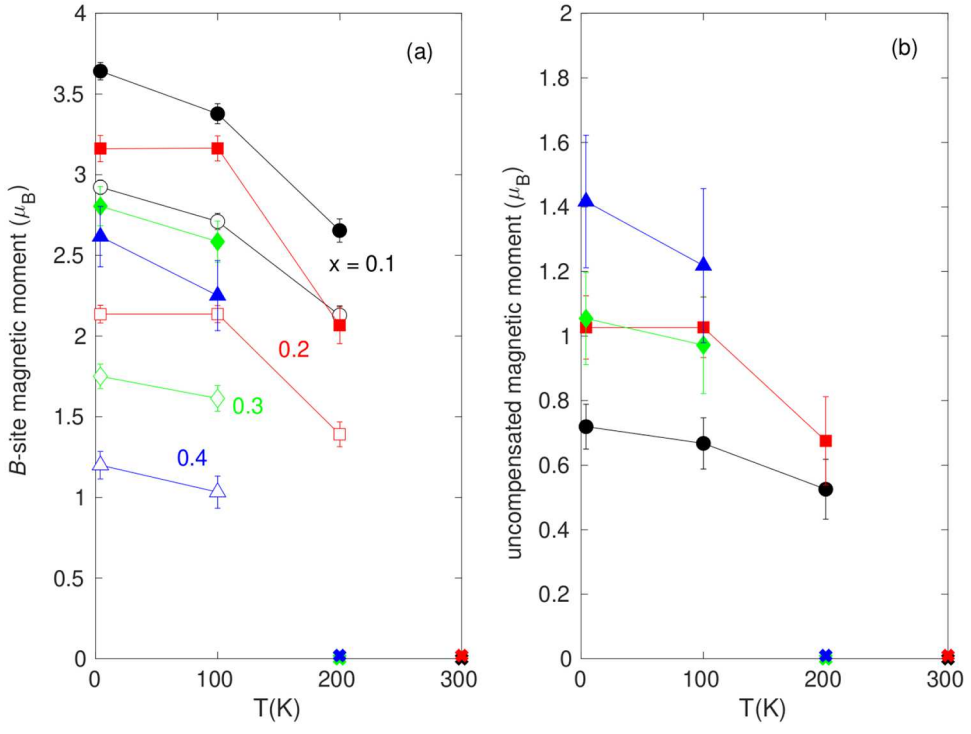

Fig. 13. (a) B-site magnetic moments extracted from NPD data for the quenched $Pb(Fe_{1-x}Sc_x)_{2/3}W_{1/3}O_3$ samples ($0.1 \leq x \leq 0.4$); filled markers: $4b$ site, open markers: $4a$ site. (b) Uncompensated moment estimated from the difference between $4b$ and $4a$ moments. No magnetic contribution was observed at $T = 300$ K for $x = 0.1$ and 0.2, and at $T = 200$ K for $x = 0.3$ and 0.4.

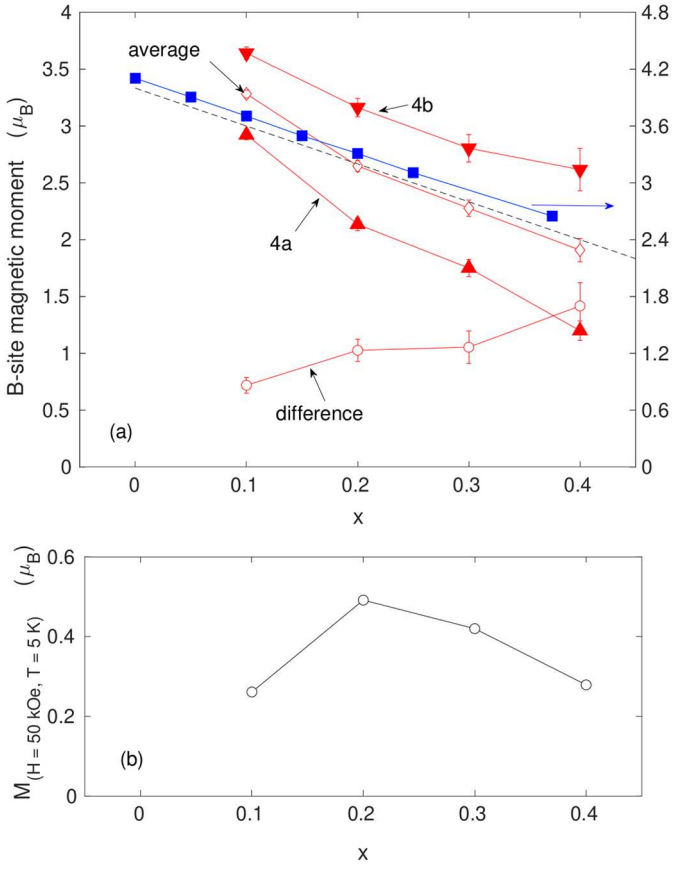

Fig. 14. (a) Magnetic moments on *4a* and *4b* sites (triangles) for the quenched $Pb(Fe_{1-x}Sc_x)_{2/3}W_{1/3}O_3$ samples ($0.1 \leq x \leq 0.4$) determined from the NPD data at 4 K, as well as their average (diamonds) and difference (circles). The theoretical estimation of the average magnetic moment on *B*-site is included using filled squares and right axis (considering only the Fe local moment, i.e. no W). The dashed black line corresponds to the dilution of the 5 μB magnetic moment of Fe^{3+} according to $\mu = 5 \times (1 - x) \times 2/3$. (b) Magnetization M(H = 50 kOe) at 5 K for the quenched $Pb(Fe_{1-x}Sc_x)_{2/3}W_{1/3}O_3$ samples ($0.1 \leq x \leq 0.4$) extracted from the magnetization vs magnetic field curves of Figure 7b.

difference of the magnetic moment on the B' and B'' sites, and thus a large excess moment and ferrimagnetic behaviour in this quenched sample, owing to the non-equivalent occupation factors of Fe on the *B*-sites (see XRD results plotted in Fig. 2a) for the quenched low-Sc doped samples.

4 Discussion

The cationic order on the *B*-site in Pb-based relaxor ferroelectric perovskites has been the subject of considerable debate [71–73]. Controversies exist regarding the composition of the cation sites and the relationship between the magnetic order and dielectric relaxor properties. It is generally accepted that ordering in complex perovskites is favoured by large differences in charge between the two *B*-site ions and by differences in ionic radii [74–76]. The general rule for *B*-site cation ordering considers the difference in oxidation state between the two *B*-site cations. When the difference in charge is larger than two, order is more likely than disorder. When the charge difference is exactly two, other factors such as cation size difference and bonding preferences must be taken into account [74]. Ionisation potentials, cation coordination geometry, and the *A*-site cation:*B*-site cation size ratio have also been mentioned as factors that influence the degree of cation ordering [74–76]. PFWO is the first MF which was discovered in the $PbB^{3+}_{2/3}B^{6+}_{1/3}O_3$ double perovskite family [7,8]. The original idea was based on the search for ferrimagnetic perovskites with some degree of order on *B*-sites, creating two sub-lattices corresponding to the formula $Pb[Fe]_{0.5}[Fe_{1/3}W_{2/3}]_{0.5}O_3$. In this case, the magnetic moments of two sub-lattices arranged antiferromagnetically are not compensated, and the ferroelectric material also becomes ferrimagnetic. A number of experimental results indicate that partial order does exist and that the correct structural formula for PFWO is $Pb[Fe_{1-x}W_x]_{0.5}[Fe_{1/3+x}W_{2/3-x}]_{0.5}O_3$ with $0 < x < 1/3$ [77]. Owing to the similar size of Fe^{3+} and W^{6+} in the case of $Pb(Fe_{2/3}W_{1/3})O_3$ (tolerance factor $t = 1.007$) is quite problematic to realize the B-site cation order. However, other members of the 2:1 tungstate family such as $Pb(Sc_{2/3}W_{1/3})O_3$ (PSWO) ($t = 0.974$) readily adopt a 1:1 ordered double perovskite structure [65–67]. Studies of the PSWO structure indicate that PSWO has a random site arrangement of cations with one site occupied by Sc^{3+} cation and the second by a random distribution of W^{6+} and the remaining Sc^{3+} cations, yielding the structural formula $Pb(Sc_{1/3}W_{2/3})_{1/2}(Sc)_{1/2}O_3$ [65–67].

The XRPD patterns of the PFSWO samples indicate that disordered structure of the annealed PFWO has a very limited range of stability in the solid solution system (up to 5% Sc). The annealed samples containing a larger concentration of Sc ($x > 0.05$) were comprised of a two-phase mixture of ordered ($Fm\bar{3}m$) and disordered ($Pm\bar{3}m$) cubic structures. The patterns collected from $x = 0.60$ and up to 1.0 could all be indexed in terms of the single-phase, cubic ($Fm\bar{3}m$) structure. For the quenched samples, this phase is stable over the full concentration range of Sc susbstitution ($0.05 \leq x \leq 1$). In ordered PFSWO perovskites, the B' position is occupied by a larger ferroelectrically "inactive" cation (Sc) and the B'' position by a smaller ferroelectrically "active" cation (W), and the intermediate oxygen anions are displaced toward the B'' position. This cooperative displacement mechanism can then result in extended ferroelectric coupling. The abnormally large atomic displacement parameters for Pb cations ($B_{Pb} = 3.5\,Å^2$) provide strong evidence for the presence of disordered atomic displacements. Such behaviour is typical for Pb-based perovskites containing Pb^{2+} on the A-site, due to the presence of a stereoactive electron lone pair on Pb^{2+} cations [78–80].

According to group theoretical prediction [81] the phase transition from $Pm\bar{3}m$ to $Fm\bar{3}m$ in perovskites is initiated by a breath-type mode at the R point of the Brillouin zone. This mode, accompanied by the formation of a nonequivalent oxygen octahedron, sequences

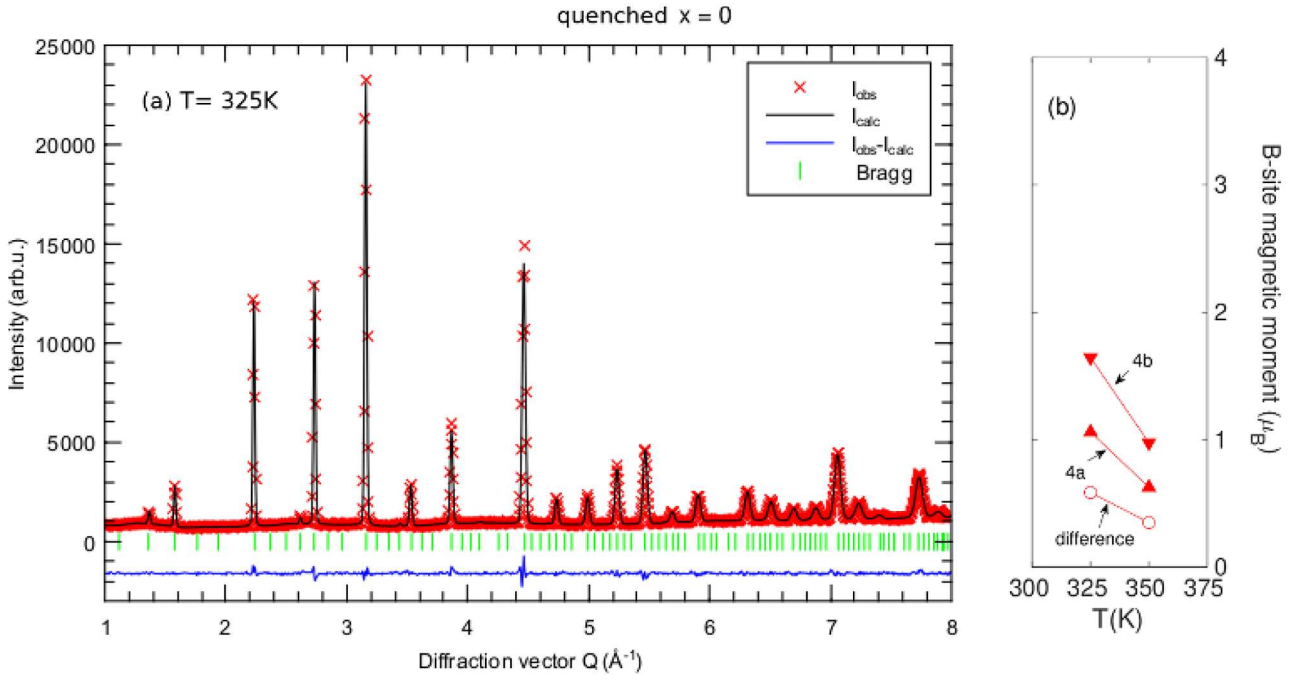

Fig. 15. (a) NPD diffractogram at $T = 325$ K and associated refinements on a quenched $x = 0$ sample (R_B: 1.37, R_p: 2.95, R_{wp}: 3.81). (b) Temperature variation of the extracted B-site magnetic moments and their difference (same legend as in previous figure). No magnetic contribution was observed at $T = 450$ K.

with the B' and B'' alternation. The actual structural mechanism of the transformation in PFWO remains unknown and important factors in triggering the $Pm\overline{3}m \overrightarrow{a}$ $Fm\overline{3}m$ transformation are still not fully clear. The transformation occurs by a dilatational mechanism owing to a uniform distortion of the simple cubic lattice by extension of the structure along the main crystallographic directions. Probably, there is no remarkable energy barrier for such a transformation because the cation coordination number is not changing. The nature of phase transformation could also be related to oxygen stoichiometry and requires additional investigation.

Our first-principle calculations confirm the ordering tendency in Sc-doped compounds, and the G-type antiferromagnetic configuration. For all Sc concentrations, different values of the magnetic moments on the *4a* and *4b* *B*-sites are observed experimentally, yielding an uncompensated moment. Accordingly, the temperature- and magnetic field-dependent magnetization curves of the compounds suggest that the antiferromagnetic state of the undoped compound is turned into a ferrimagnetic one upon doping. Such excess moments may appear even in the undoped compound under suitable thermal procedure. It is known that in complex metal oxides with perovskite structure quenching can be a very useful tool to retain the structure obtained at high temperature and prevent degradation of the structure during slow cooling [17]. Besides, the appearance of structural defects is different affecting the structure and final multifunctional properties (dielectric, ferroelectric, or magnetic). For those and many other reasons, thermal treatements such as quenching can change the behaviour of materials including crystal, real structure, and physical properties. Partial cation ordering in $Pb(Fe_{2/3}W_{1/3})O_3$ prepared under specific oxygen atmosphere was discussed earlier [82,83], in the light of the appearance of superstructure reflections in XRPD and signature of two magnetic sublattices for the Fe^{3+} cations in Mössbauer spectra [82]. Recently, the effects of quenching on the dielectric properties of relaxor ceramics such as PLZT and BNT–$BaTiO_3$ systems have been reported, and they suggest that quenching could be a promising method to improve the dielectric ageing effect and other thermal behaviours in relaxor ferroelectrics [84–86].

5 Conclusions

Phase pure solid solutions $Pb(Fe_{1-x}Sc_x)_{2/3}W_{1/3}O_3$ were synthesized using a conventional solid-state reaction method. (S)XRPD, NPD, dielectric and magnetic measurements, thermogravimetric analysis, scanning electron microscopy (SEM), energy dispersive X-ray, Mossbauer spectroscopy, and first-principles calculations were used as analytical tools.

It is found that even quite small concentrations of Sc ($x = 0.05$) cause ordering of the cations and stabilization in the $Fm\overline{3}m$ structure. For quenched samples, this phase is stable over the full concentration range of Sc substitution ($0.05 \leq x \leq 1$). This partial positional order of PFSWO does not produce perfect compositional order, and one sub-lattice remains disordered. However, the ordering produces unbalanced magnetic sub-lattices and ferrimagnetic behaviour below the magnetic ordering temperature. The excess moment of this phase is found to be controlled by the amount of Sc substitution and the final thermal treatment of the sample preparation. All the

attempts to transform the relaxor properties of PFWO by Sc doping to ferroelectric ordering have invariably failed, leaving its diffuse dielectric phase transitions an enigma.

Financial support from the Russian Foundation for Basic Research (grant RFBR 18-03-00245) and the Swedish Research Council (VR) is gratefully acknowledged. Parts of this research were carried out at the light source PETRA III (beamline P02.1) at DESY, a member of the Helmholtz Association (HGF). Neutron powder diffraction measurements were carried out at the CANAM infrastructure of the NPI CAS Rez supported through the Ministry of Education, Youth and Sports project No. LM2015056 and project LM2015074.

Author contribution statement

S.A.I. designed the research and prepared a first draft of the manuscript. S.A.I., P.B., S.S., M.S. and R.T. performed the synthesis, chemical analysis and collected and analysed the diffraction data. A.A.B. was responsible for dielectric data collection and analysis, and T.S., P.N. and R.M. for the magnetic data collection and analysis, while D.W., B.S.,Ya.K., and O.E. were in charge of the first principles calculations. All authors contributed to the writing of the manuscript.

References

1. M.M. Vopson, Crit. Rev. Solid State Mater. Sci. **40**, 223 (2015)
2. B. Wang, *Mechanics of Advanced Functional Materials. Advanced Topics in Science and Technology in China* (Springer, Berlin, Heidelberg, 2013)
3. K.F. Wang, J.M. Liu, Z.F. Ren, Adv. Phys. **58**, 321 (2009)
4. H. Liu, X. Yang, Ferroelectrics **507**, 69 (2017)
5. I.E. Chupis, Low Temp. Phys. **36**, 477 (2010)
6. S. Vasala, M. Karppinen, Prog. Solid State Chem. **43**, 1 (2015)
7. G.A. Smolenski, A.I. Agranovskaya, V.A. Isupov, Sov. Phys. Sol. State **1**, 907 (1959)
8. G.A. Smolenskii, J. Phys. Soc. Jpn. (Suppl.) **28**, 26 (1970)
9. L.E. Cross, Ferroelectrics **76**, 241 (1987)
10. A.A. Bokov, Z.G. Ye, J. Mater. Sci. **41**, 31 (2006)
11. A. Levstik, Appl. Phys. Lett. **91**, 012905 (2007)
12. I.W. Chen, J. Phys. Chem. Solids **61**, 197 (2000)
13. L. Chen, A.A. Bokov, W. Zhu, H. Wu, J. Zhuang, Z.G. Ye, Sci. Rep. **6**, 22327 (2016)
14. Y. Shimakawa, M. Azuma, N. Ichikawa, Materials **4**, 153 (2011)
15. S. Matteppanavar, S. Rayaprol, A.A. Angadi, B. Sahoo, Ceram. Int. **41**, 11680 (2015)
16. J.F. Scott, NPG Asia Mater. **5**, e72-11 (2013)
17. Y.N. Venevtsev, E.D. Politova, S.A. Ivanov, in *Ferro- and Antiferroelectrics of Barium Titanate Family, Chemistry* (Moscow, 1985), p. 256
18. Yu. N. Venevtsev, V.V. Gagulin, V.N. Ljubimov, in *Ferroelectromagnets* (Nauka, Moscow, 1982), p. 172
19. L. Zhou, P.M. Vilarinho, P.Q. Mantas, J.L. Baptista, E. Fortunato, J. Eur. Ceram. Soc. **20**, 1035 (2000)
20. S.A. Ivanov, Magnetoelectric complex metal oxides: main features of preparation, structure and properties, in *Advanced Functional Materials*, edited by B. Sanyal, O. Eriksson (Elsevier, Oxford, UK, 2012), pp. 163–234
21. R.N.P. Choudhary, D.K. Pradhan, C.M. Tirado, G.E. Bonilla, R.S. Katiyar, Phys. Status Solidi B **244**, 2254 (2007)
22. Y.A. Shevchuk, S.K. Korchagina, V.V. Gagulin, V.V. Bogatko, Ferroelectrics **199**, 223 (1997)
23. B. Fraygola, J.A. Eiras, Mater. Res. **17**, 1594 (2014)
24. D. Lee, S.M. Yang, Y. Jo, T.K. Song, J. Korean Phys. Soc. **57**, 1914 (2010)
25. M. Yokosuka, H. Kojima, Jpn. J. Appl. Phys. **36**, 6046 (1997)
26. S.A. Ivanov, P. Nordblad, R. Tellgren, T. Ericsson, H. Rundlöf, Solid State Sci. **9**, 440 (2007)
27. D. Szwagierczak, J. Kulawik. J. Eur. Ceram. Soc. **25**, 1657 (2005)
28. L. Zhou, P.M. Vilarinho, J.L. Baptista, J. Appl. Phys. **85**, 2312 (1999)
29. D. Brzezinska, R. Skulski, D. Bochenek, P. Niemiec, A. Chrobak, L. Fajfrowski, S. Matyjasik, J. Alloys Compd. **737**, 299 (2018)
30. C. Miranda, P.M. Vilarinho, L.Q. Zhou, Ferroelectrics **223**, 269 (1999)
31. B.H. Lee, N.K. Kim, B.O. Park, S.H. Cho, Mater. Lett. **33**, 57 (1997)
32. A.S. Khim, J. Wang, X. Junmin, Solid State Ionics **127**, 285 (2000)
33. K. Uchino, S. Nomura, J. Phys. Soc. Jpn. **41**, 542 (1976)
34. K. Uchino, S. Nomura, Jpn. J. Appl. Phys. **18**, 1493 (1979)
35. S.A. Ivanov, A.A. Bush, C. Ritter, M.A. Behtin, V.M. Cherepanov, C. Autieri, Y.O. Kvashnin, I. Di Marco, B. Sanyal, O. Eriksson, P. Anil Kumar, P. Nordblad, R. Mathieu, Mater. Chem. Phys. **187**, 218 (2017)
36. S. Matteppanavar, S. Rayaprol, B. Angadi, B. Sahoo, J. Supercond. Novel Magn. **30**, 1317 (2017)
37. S. Matteppanavar, S. Rayaprol, B. Angadi, B. Sahoo, J. Alloys Compd. **677**, 27 (2016)
38. P.M. Vilarinho, L. Zhou, M. Pöckl, N. Marques, J.L. Baptista, J. Am. Ceram. Soc. **83**, 1149 (2000)
39. L. Feng, H. Guo, Z.G. Ye, J. Mater. Res. **22**, 2116 (2006)
40. E. Dulkin, E. Mojaev, M. Roth, S. Kamba, P.M. Vilarinho, J. Appl. Phys. **103**, 083542 (2008)
41. R. Wongmaneerung, X. Tan, R.W. McCallum, S. Ananta, R. Yimnirun, Appl. Phys. Lett. **90**, 242905 (2007)
42. X. Tan, R. Wongmaneerung, R.W. McCallum, J. Appl. Phys. **102**, 104114 (2007)
43. Z.G. Ye, K. Toda, M. Sato, J. Korean Phys. Soc. **32**, S1028 (1998)
44. S.A. Ivanov, S.-G. Eriksson, R. Tellgren, H. Rundlöf, Mater. Res. Bull. **39**, 2317 (2004)
45. B. Fraygola, A. Mesquita, A.A. Coelho, D. Garcia, V.R. Mastelaro, J.A. Eiras, Phys. Status Solidi A **210**, 386 (2013)

46. Z.G. Ye, H. Schmid, J. Cryst. Growth **167**, 628 (1996)
47. A.F. Koroleva, A.A. Bush, K.E. Kamentsev, V.Ya. Shkuratov, S.A. Ivanov, V.M. Cherepanov, S. Shafeie, Inorg. Mater. **54**, 288 (2018)
48. G.A. Komandin, O.E. Porodinkov, A.A. Bush, A.F. Koroleva, I.E. Spektor, S.V. Chuchupal, D.S. Seregin, L.D. Iskhakova, Phys. Solid State **59**, 2365 (2017)
49. J. Rodriguez-Carvajal, Physica B **192**, 55 (1993)
50. A.C. Dippel, H.P. Liermann, J.T. Delitz, P. Walter, H. Schulte-Schrepping, O.H. Seeck, H. Franz, J. Synchrotron Radiat. **22**, 675 (2015)
51. A.P. Hammersley, S.O. Svensson, M. Hanfland, A.N. Fitch, D. Hausermann, High Pressure Res. **14**, 235 (1996)
52. V.F. Sears, Neutron News **3**, 26 (1992)
53. M.I. Aroyo, J.M. Perez-Mato, D. Orobengoa, E. Tasci, G. de la Flor, A. Kirov, Bulg. Chem. Commun. **43**, 183 (2011)
54. A.S. Kamzin, V.A. Bokov, Phys. Solid State **55**, 1191 (2013)
55. G. Kresse, J. Furthmüller, Phys. Rev. B **54**, 11169 (1996)
56. G. Kresse, D. Joubert, Phys. Rev. B **59**, 1758 (1999)
57. J.P. Perdew, K. Burke, M. Ernzerhof, Phys. Rev. Lett. **77**, 3865 (1996)
58. A.I. Liechtenstein, V.I. Anisimov, J. Zaanen, Phys. Rev. B **52**, R5467 (1995)
59. V.I. Anisimov, F. Aryasetiawan, A.I. Lichtenstein, J. Phys.: Condens. Matter **9**, 767 (1997)
60. G. Rollmann, A. Rohrbach, P. Entel, J. Hafner, Phys. Rev. B **69**, 165107 (2004)
61. R.D. Shannon, Acta Crystallogr. A **32**, 751 (1976)
62. K. Momma, F. Izumi, J. Appl. Crystallogr. **44**, 1272 (2011)
63. C.G. Stenger, A.J. Burggraaf, Phys. Status Solidi A **61**, 653 (1980)
64. D.J. Goossens, Acc. Chem. Res. **46**, 2597 (2013)
65. P. Juhas, I. Grinberg, A.M. Rappe, W. Dmowski, T. Egami, P.K. Davies, Phys. Rev. B **69**, 214101 (2004)
66. P. Juhas, P.K. Davies, M.A. Akbas, AIP Conf. Proc. **626**, 108 (2002)
67. P. Juhas, P.K. Davies, M.A. Akbas, J. Am. Ceram. Soc. **87**, 2086 (2004)
68. J. Blasco, C. Ritter, L. Morellon, P.A. Algarabel, J.M. De Teresa, D. Serrate, J. García, M.R. Ibarra, Solid State Sci. **4**, 651 (2002)
69. J.B. Goodenough, J. Phys. Chem. Solids **6**, 287 (1958)
70. J. Kanamori, J. Phys. Chem. Solids **10**, 87 (1959)
71. P. Davies, H. Wu, A. Borisevich, I. Molodetsky, L. Farber, Annu. Rev. Mater. Res. **38**, 369 (2008)
72. L. Zhou, P.M. Vilarinho, J.L. Baptista, J. Eur. Ceram. Soc. **18**, 1383 (1998)
73. N. Setter, L.E. Cross, J. Appl. Phys. **51**, 4356 (1980)
74. G. King, P.M. Woodward, J. Mater. Chem. **20**, 5785 (2010)
75. M.W. Lufaso, P.M. Woodward, Acta Cryst. Sect. B **60**, 10 (2004)
76. M.T. Anderson, K.B. Greenwood, G.A. Taylor, K.R. Poeppelmeier, Prog. Solid State Chem. **22**, 197 (1993)
77. V.A. Isupov, Ferroelectrics **315**, 149 (2005)
78. S.A. Larregola, J.A. Alonso, M. Alguero, R. Jimenez, E. Suard, F. Porcher, J.C. Pedregosa, Dalton Trans. **39**, 5159 (2010)
79. B. Malibert, M. Dkhil, M. Dunlop, J.M. Kiat, G. Baldinozzi, S.B. Vakhrushev, Ferroelectrics **235**, 87 (1999)
80. J.A. Alonso, I. Rasines, J. Phys. Chem. Solids **49**, 3885 (1988)
81. K.S. Aleksandrov, S.V. Misyul, E.E. Baturinets, Ferroelectrics **354**, 60 (2007)
82. Yu.N. Venevtsev, V.V. Sklyarevskii, I.I. Lukashevich, V.P. Romanov, N.M. Kotov, A.I. Kashlinskii, N.I. Filipov, A.S. Viskov, Sov. Phys. Crystallogr. **21**, 556 (1976) [original article (in Russian): Kristallografiya **21**, 971 (1976)]
83. I.P. Raevskii, D.A. Sarychev, S.A. Bryugeman, L.A. Reznichenko, L.A. Shilkina, O.N. Razumovskaya, V.S. Nikolaev, N.P. Vyshatko, A.N. Salak, Crystallogr. Rep. **47**, 1012 (2002) [original article (in Russian): Kristallografiya **47**, 1081 (2002)]
84. J. Zang, W. Jo, J. Rödel, Appl. Phys. Lett. **102**, 032901 (2013)
85. H. Muramatsu, H. Nagata, T. Taken, Jpn. J. Appl. Phys. **55**, 10TB07 (2016)
86. Y.C. Hu, Y.W. Cui, X.W. Wang, Y.P. Liu, Chin. Phys. Lett. **33**, 026101 (2016)